

Competition of shape and interaction patchiness for self-assembling nanoplates

Xingchen Ye^{1†}, Jun Chen^{2†}, Michael Engel^{4†}, Jaime A. Millan^{5†}, Wenbin Li⁶, Liang Qi⁷, Guozhong Xing³, Joshua E. Collins⁸, Cherie R. Kagan^{1,2,3}, Ju Li^{6,7}, Sharon C. Glotzer^{4,5*} and Christopher B. Murray^{1,2*}

Progress in nanocrystal synthesis and self-assembly enables the formation of highly ordered superlattices. Recent studies focused on spherical particles with tunable attraction and polyhedral particles with anisotropic shape, and excluded volume repulsion, but the effects of shape on particle interaction are only starting to be exploited. Here we present a joint experimental-computational multiscale investigation of a class of highly faceted planar lanthanide fluoride nanocrystals (nanoplates, nanoplatelets). The nanoplates self-assemble into long-range ordered tilings at the liquid-air interface formed by a hexane wetting layer. Using Monte Carlo simulation, we demonstrate that their assembly can be understood from maximization of packing density only in a first approximation. Explaining the full phase behaviour requires an understanding of nanoplate-edge interactions, which originate from the atomic structure, as confirmed by density functional theory calculations. Despite the apparent simplicity in particle geometry, the combination of shape-induced entropic and edge-specific energetic effects directs the formation and stabilization of unconventional long-range ordered assemblies not attainable otherwise.

Nanocrystals often exhibit well-defined facets that result in a three-dimensional (3D) polyhedral shape^{1–5} or, if crystal growth is suppressed in one direction, in a polygonal two-dimensional (2D) shape^{4–7}. The assembly of such faceted particles is dominated by driving forces that maximize face-to-face (or, in 2D, edge-to-edge) contact, which is both energetically and entropically favoured. Similar to crystals of spherical colloids dominated by interparticle interactions^{8–13}, even perfectly hard nanocrystals can order without explicit attractive interactions at high-enough densities^{14–24}; recent simulations predict a rich diversity of entropically stabilized nanocrystal superlattices²⁵.

Inherent attractive forces between nanocrystals can add further complexity to their assembly. To grow and stabilize nanocrystals in solution, they are coated with ligand molecules^{6,7}, which interact via hydrocarbon chains to generate an effective attraction between the nanocrystals. As crystallographically distinct facets and edges have different atomic structure and density of cationic sites, they can have different densities of ligand molecules and therefore different strength and range of interactions with other facets and edges. Such patchiness of the ligand shell was observed with DNA surface-bound ligands on gold nanoprisms^{26,27} and with oleic acid on PbSe nanocrystals²⁸, but is not yet exploited for the self-assembly of nanocrystal superlattices.

The delicate balance between entropic and energetic effects in complex self-assembly processes was highlighted in systems of supramolecular rhombi adsorbed on graphite^{29–31}. In a similar fashion, complex crystalline assemblies should also be obtainable on a larger scale through rational and predictive design by combining entropic and interaction patchiness made possible by the unique shape of nanocrystals. As a demonstration of this fundamental principle,

we investigated the spontaneous organization of nanoplates into planar superstructures in a hexane wetting layer at the liquid-air interface. We chose lanthanide fluoride (LnF_3) nanocrystals as model systems because of their diverse anisotropic crystal structures and recent advances in the synthesis of LnF_3 nanomaterials^{4,6,32}. A systematic study of nanocrystal growth reveals a correlation between nanocrystal phase stability and lanthanide contraction, which yields a series of monodisperse faceted nanocrystals that include circular, rhombic and irregular hexagonal plates, as well as tetragonal bipyramids. We demonstrate that the rhombic and irregular hexagonal nanoplates represent a fascinating class of planar nanotiles that exhibit rich and subtle phase behaviour.

Results and discussion

Synthesis. Nanocrystals were synthesized by rapid thermal decomposition of lanthanide trifluoroacetate precursors in the presence of oleic acid as a colloidal stabilizer (Fig. 1a). The choice of lanthanide elements and the addition of lithium trifluoroacetate or LiF salts control the nanocrystal composition and the evolution of nanocrystal shape. For lighter Ln^{3+} ions (from La to Sm) with larger ionic radii, LnF_3 nanocrystals adopt the trigonal tyanite structure and produce circular nanoplates (Fig. 1d and Supplementary Figs S1 and S2). However, for heavier Ln^{3+} ions (from Er to Lu), LiLnF_4 (tetragonal scheelite structure) nanocrystals with a tetragonal-bipyramidal shape are formed (Supplementary Figs S3 and S4). In the middle of the lanthanide series ($\text{Ln} = \text{Eu-Dy}$), irregular hexagonal nanoplates with the orthorhombic $\beta\text{-YF}_3$ structure (space group $Pnma$) are produced, as confirmed by powder X-ray diffraction (XRD) patterns (Fig. 1c and Supplementary Figs S5–S15). High-resolution transmission

¹Department of Chemistry, University of Pennsylvania, Philadelphia, Pennsylvania 19104, USA, ²Department of Materials Science and Engineering, University of Pennsylvania, Philadelphia, Pennsylvania 19104, USA, ³Department of Electrical and Systems Engineering, University of Pennsylvania, Philadelphia, Pennsylvania 19104, USA, ⁴Department of Chemical Engineering, University of Michigan, Ann Arbor, Michigan 48109, USA, ⁵Department of Materials Science and Engineering, University of Michigan, Ann Arbor, Michigan 48109, USA, ⁶Department of Materials Science and Engineering, Massachusetts Institute of Technology, Cambridge, Massachusetts, 02139, USA, ⁷Department of Nuclear Science and Engineering, Massachusetts Institute of Technology, Cambridge, Massachusetts, 02139, USA, ⁸Intelligent Material Solutions, Inc., Princeton, New Jersey 08540, USA; [†]These authors contributed equally to this work. *e-mail: sglotzer@umich.edu; cbmurray@sas.upenn.edu

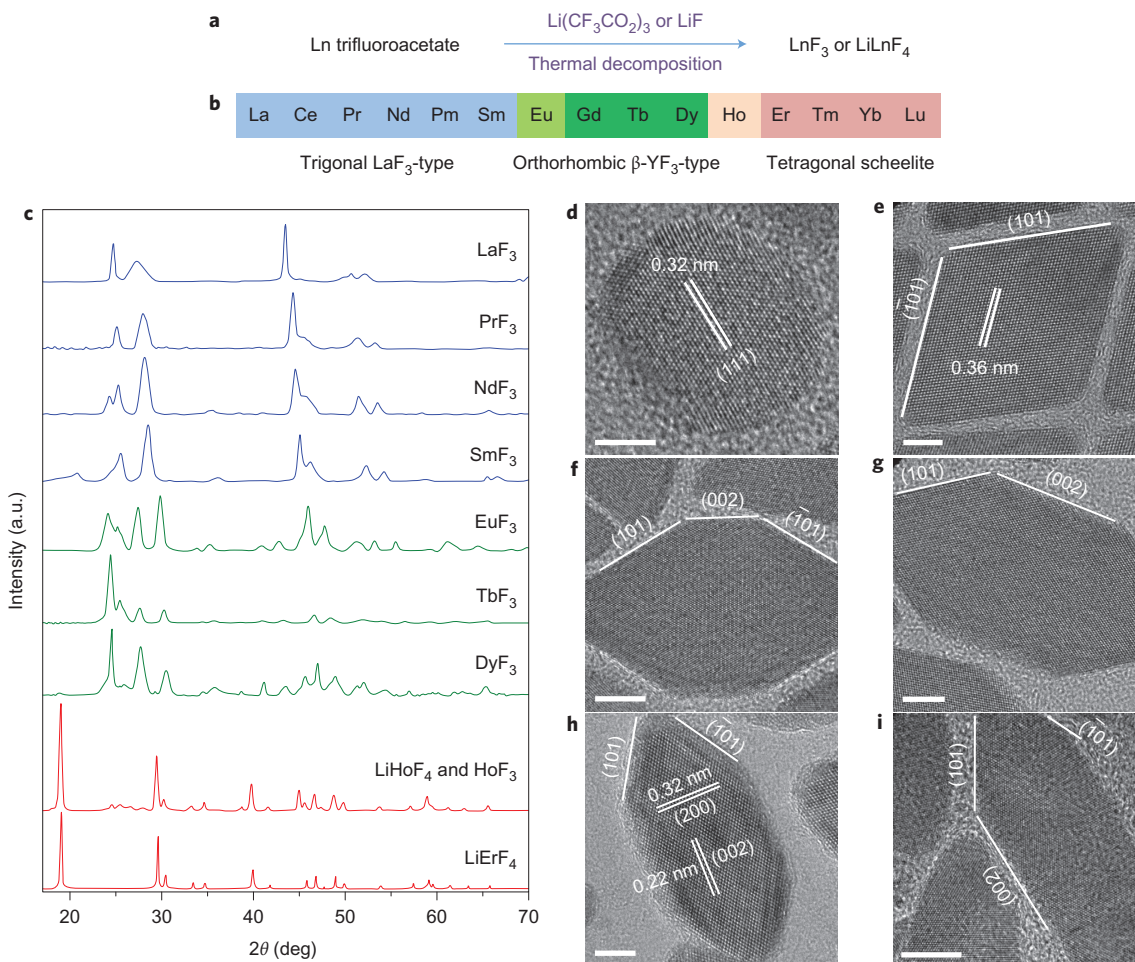


Figure 1 | Synthesis and structural characterization of monodisperse lanthanide fluoride nanocrystals. **a**, Schematic representation of the synthesis method. **b**, General trend of stable phases from trigonal LnF_3 to orthorhombic LnF_3 and to tetragonal LiLnF_4 phases as a function of the type of lanthanide ions. Experimental results for Eu^{3+} and Ho^{3+} show the possibility of coexisting phases. **c**, Powder XRD patterns of different LnF_3 and LiLnF_4 nanocrystals. **d–i**, HRTEM images of NdF_3 (**d**), DyF_3 (**e**), TbF_3 (**f**), DyF_3 (**g**) and EuF_3 (**i**) nanoplates. Scale bars (**d**, **e**, **h**), 5 nm; (**f**, **g**, **i**), 10 nm.

electron microscopy (HRTEM) images show that each nanoplate comprises four symmetry-equivalent edges ($\{101\}$ facets) at the tips with an apex angle of $68^\circ \pm 0.5^\circ$, separated by two $\{002\}$ side facets in the middle (Fig. 1f–i). The plate shape was further confirmed by HRTEM images of nanoplates standing edge-on (Supplementary Fig. S9). The Ln^{3+} ions dominated the $\{010\}$ planes and therefore we postulate that nanocrystal growth along the $\langle 010 \rangle$ direction was retarded because of the oleic acid coordination of lanthanide cations, which gave rise to the plate morphology. Although systems of four-sided rhombs in supramolecular tilings^{29–31} and polymeric platelets fabricated by photolithography³³ have been studied before, the irregular six-sided geometry of LnF_3 nanoplates has not yet been reported. Our results overlap with these works only in the boundary case of the 68° rhomb (Fig. 1e).

The lateral dimensions of the irregular hexagonal nanoplates can be adjusted by the choice of lanthanide elements and nanocrystal growth conditions, with the plate thickness kept between 4.5 and 7.0 nm. The lanthanide contraction determines the lanthanide fluoride phase stability: lighter Ln^{3+} ions with larger ionic radii favour a higher coordination number, as evidenced by the eleven fluoride ions that surround each Ln^{3+} ion in the trigonal LaF_3 -type structure. As the atomic number of the lanthanide increases, crystal structures that feature lower coordination numbers of nine (orthorhombic $\beta\text{-YF}_3$ type) or eight (tetragonal LiYF_4 type) dominate³⁴, which reflects the effect of cation size and polarizability³².

Interfacial self-assembly. To study the shape-directed packing behaviour of nanoplates, an interfacial assembly strategy was employed^{4,35}. The viscous polar ethylene glycol subphase provided individual nanoplates of sufficient mobility, even at high particle-volume fractions, to anneal out defects and access thermodynamically stable assemblies over extended areas. Face-to-face stacked superstructures are observed in many plate-like colloids^{2,6,7,36,37} and are often rationalized on the basis of maximization of local packing fraction and van der Waals interactions between neighbouring plates. In this work, the nanoplate concentration in the spreading solution was adjusted carefully to ensure that uniform planar 2D superstructures dominated (Supplementary Fig. S16). The as-synthesized nanoplates were subjected to several rounds of purification steps using a solvent/non-solvent combination to minimize the amount of free oleic acid molecules that may act as depletants and induce lamellar face-to-face stacking during self-assembly.

A library of 2D superlattices self-assembled from rhombic and irregular hexagonal nanoplates of different aspect ratios is shown in Fig. 2. For rhombic nanoplates, the superlattices display cmm symmetry as manifested by the small-angle electron-diffraction pattern (Fig. 2a and Supplementary Fig. S17). The clear-cut edges allow the nanoplates to be crystallographically registered in the superlattices, as confirmed by the bright spots in the wide-angle electron-diffraction pattern that arises from the periodicity of

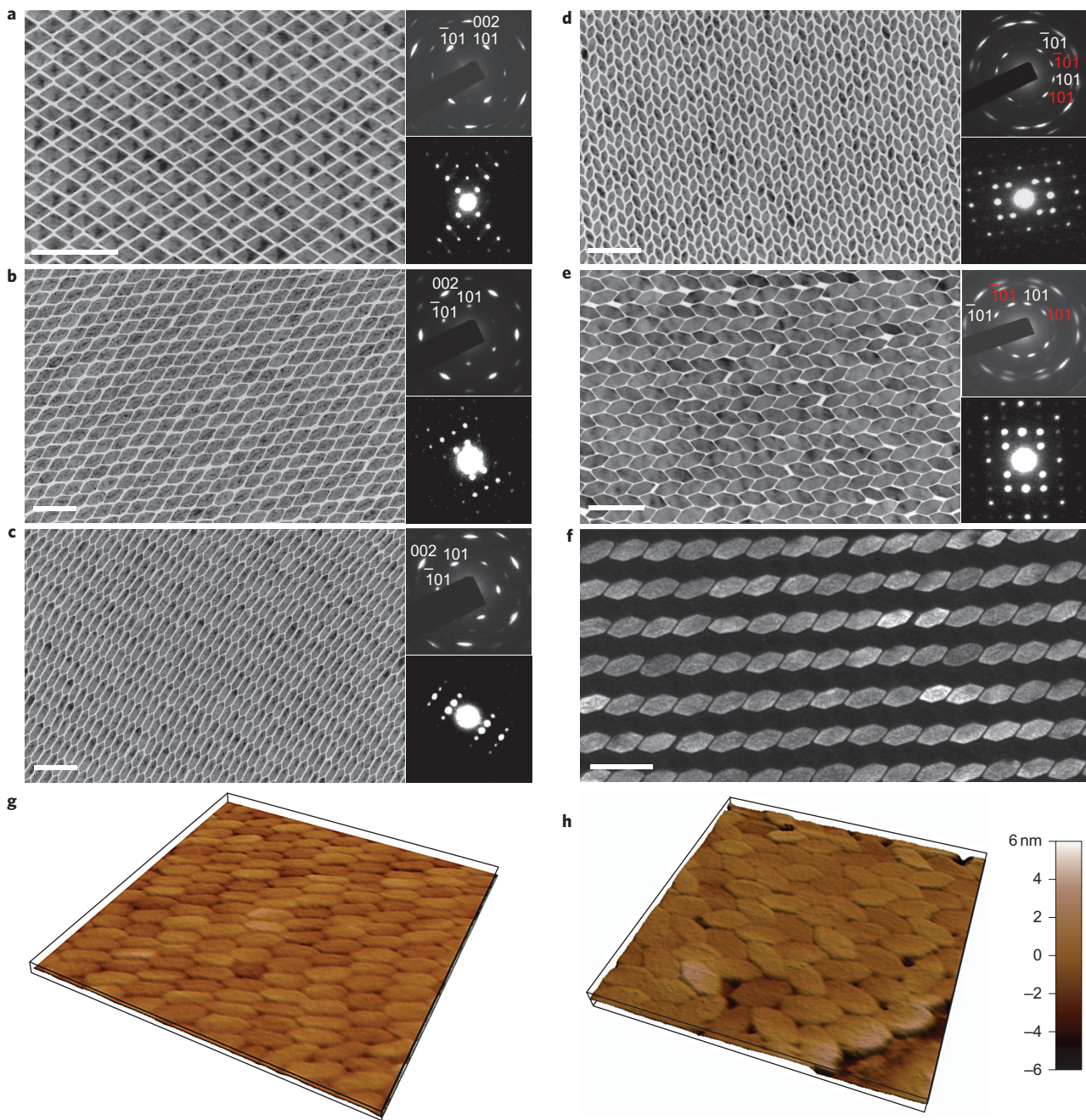


Figure 2 | 2D superlattices self-assembled from lanthanide fluoride nanoplates. **a–c**, Parallel arrangements of DyF₃ rhombohedral nanoplates (**a**), small aspect ratio TbF₃ hexagonal nanoplates (**b**) and EuF₃ large aspect ratio hexagonal nanoplates (**c**). **d,e**, Alternating arrangements of intermediate aspect ratio hexagonal nanoplates of composition DyF₃ (**d**) and TbF₃ (**e**); for each, TEM images are shown on the left, and wide-angle and small-angle (upper right and lower right, respectively) electron-diffraction patterns. **f**, Dark-field TEM image of the same area as shown in (**e**). Scale bars, **a–f**, 100 nm. **g,h**, AFM 3D topography images of EuF₃ (**g**) and TbF₃ (**h**) nanoplate superlattices. The scan sizes are 450 nm × 450 nm (**g**) and 500 nm × 500 nm (**h**).

atomic lattice planes. Moreover, point defects or stacking faults are commonly seen in the rhombic nanoplate superlattice (Supplementary Fig. S34), which was predicted by simulations of random rhombus tiling^{31,38}, and observed experimentally in molecular rhombus tilings²⁹. Further symmetry breaking of the nanoplate's shape anisotropy from rhombus to irregular hexagon offers dramatic packing precision. For nanoplates with either a short or long middle segment (<{002} side facets) relative to the tip dimension (<{101} side facets>), we observed only a parallel arrangement in which nanoplates pack densely and preferentially align along their [100] axis (Fig. 2b,c,g and Supplementary Figs S18–S21).

However, for nanoplates with an intermediate middle segment, a striking alternating arrangement that resembles a herringbone packing occurred exclusively. Examples are DyF₃ and TbF₃ nanoplates that are similar in aspect ratio but differ in overall dimensions (Fig. 2d,e,h and Supplementary Figs S22–S25). The simultaneous in-plane positional and orientational ordering of the irregular hexagonal nanoplate superlattices is also reflected in the corresponding electron-diffraction patterns and, more remarkably, in the dark-field TEM image of the TbF₃ nanoplate superlattice, in which only one set of evenly spaced linear chains of orientationally invariant nanoplates is visible (Fig. 2f). Therefore, unprecedented control

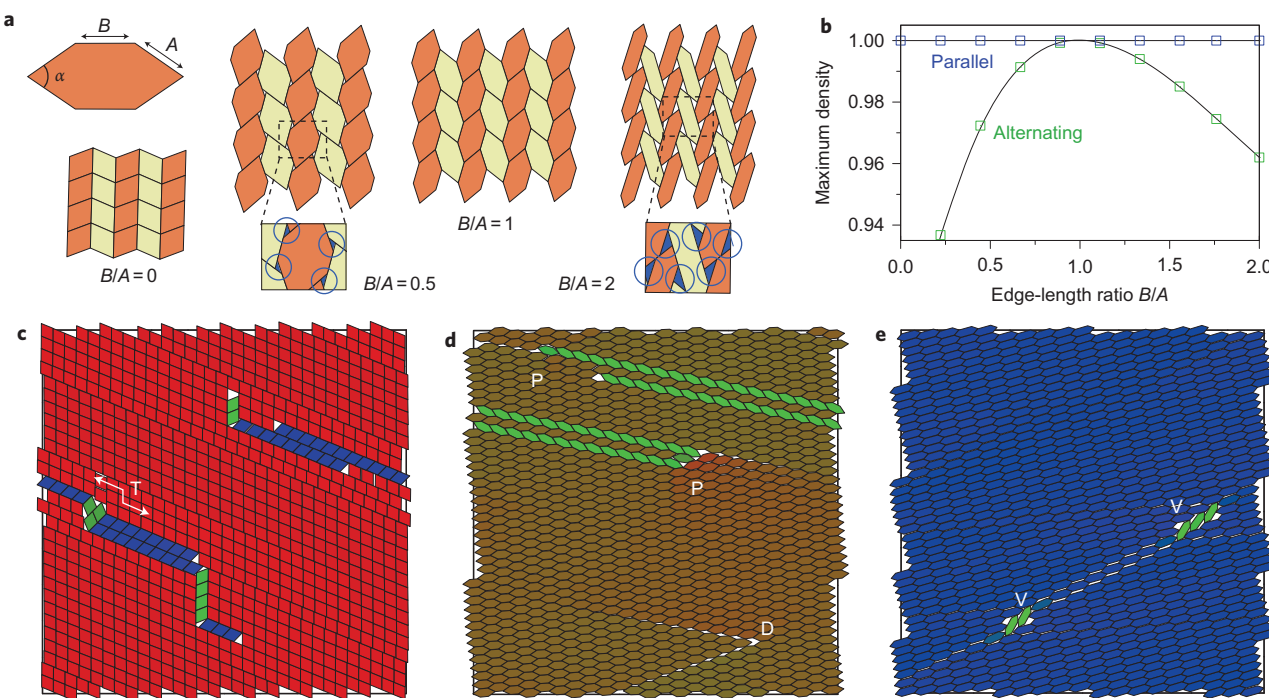


Figure 3 | Monte Carlo simulations of hard polygonal plates. **a**, The geometry of the particles is characterized by the opening angle $\alpha = 68^\circ$ and the two edge lengths A and B parallel to (101) and (001) , respectively. **b**, Alternating arrangements are only space filling for $B/A = 0$ and $B/A = 1$, and otherwise have voids. This is apparent in the densest packings as a function of the aspect ratio. Parallel arrangements are always space filling. **c-e**, Final particle configurations assembled in simulation from disordered starting configurations. The particles assemble into the parallel arrangement for all choices of the edge ratio; shown are $B/A = 0$ (**c**), $B/A = 1$ (**d**) and $B/A = 2$ (**e**). Owing to the periodic boundary conditions, structural defects in the form of twin layer (T), partial dislocations (P), dislocation (D) and vacancies (V) remained in the system. Similar defects are also frequently observed in experiments.

over shape monodispersity of the LnF_3 nanoplates provided a unique opportunity to apply shape anisotropy for directing assembly along a preferred pathway.

Monte Carlo simulation of hard plates. To identify the physical mechanism that drives the assembly, we performed Monte Carlo computer simulations of nanoplates constrained to a 2D plane. Such a constraint mimics the experimental conditions during the final stage of the hexane-evaporation process, which we interpret as follows. A thin layer of hexane on top of the ethylene glycol solubilizes the nanoplates before the hexane is dried completely. When the thickness of the hexane layer as it evaporates becomes comparable to the largest dimension of an individual nanoplate, the plates are forced to orient horizontally. As the nanoplates do not clump together face-to-face (maximizing contact) prior to the formation of a single layer, there are probably no strong attractions between them. Only when the hexane layer evaporates further and pushes the nanoplates together are they close enough for their tethers (oleic acid ligands) to interact strongly. This picture is supported by the observation that when the nanoplate concentration is increased in the spreading solution, lamellar face-to-face stacking becomes the dominant structure (Supplementary Fig. S16).

The geometry of the nanoplates is an elongated hexagon characterized by two parameters, the opening angle α and the edge-length ratio B/A (Fig. 3a). Although the angle is fixed to $\alpha = 68^\circ$ by the crystallographic relationships among the nanocrystal facets in the orthorhombic LnF_3 structure, the edge-length ratio can be varied from a degenerate rhomb ($B/A = 0$) to the equilateral elongated hexagon ($B/A = 1$) and a strongly elongated hexagon ($B/A = 2$) through the choice of lanthanide elements and nanocrystal growth conditions.

To a first approximation, we considered plates without interaction except excluded volume effects. Hard-particle systems maximize entropy during equilibration at constant volume. In the limit of high pressure the plates maximized packing, because the pressure term dominated the entropy term in the Gibbs free energy. Although elongated hexagons can fill space for all aspect ratios, the tilings were not always unique. Two candidate structures competed. For all values of B/A , the parallel arrangement was space filling. Alternating arrangements were space filling only for $B/A = 0$ and $B/A = 1$ with relative particle rotations of α and $\alpha/2$, respectively. For other edge-length ratios, small voids remained between the plates (Fig. 3a,b).

We simulated the self-assembly of hard elongated hexagons by slowly compressing the disordered fluid. The compression was chosen to mimic the conditions present during the evaporation process responsible for nanoplate assembly in experiments. We observed that elongated hexagons of all aspect ratios assembled exclusively into single crystals that corresponded to the parallel arrangement with few point defects and stacking faults (Fig. 3c-e, Supplementary Figs S26-S29 and Supplementary Movies S1-S3). The 68° opening angle of the rhombs is important for an efficient alignment. For comparison, experiments of rhomb-shaped molecular tiles with an opening angle of 60° on graphite surfaces showed a strong tendency to form a random hexagonal tiling^{29,30}. Indeed, when we simulated 60° rhombs, only random tilings were observed. The preference of the parallel arrangement was confirmed by free-energy calculations. We obtained free-energy differences of $F_{\text{alt}} - F_{\text{para}} = (0.047 \pm 0.005)k_{\text{B}}T$ for both $B/A = 0$ and $B/A = 1$ (Supplementary Fig. S30). The differences depend only slightly on packing fraction and are only 3% of the entropy jump $(T\Delta S)_{\text{melt}} = (P\Delta V)_{\text{melt}} = (1.7 \pm 0.1)k_{\text{B}}T$ during melting for the

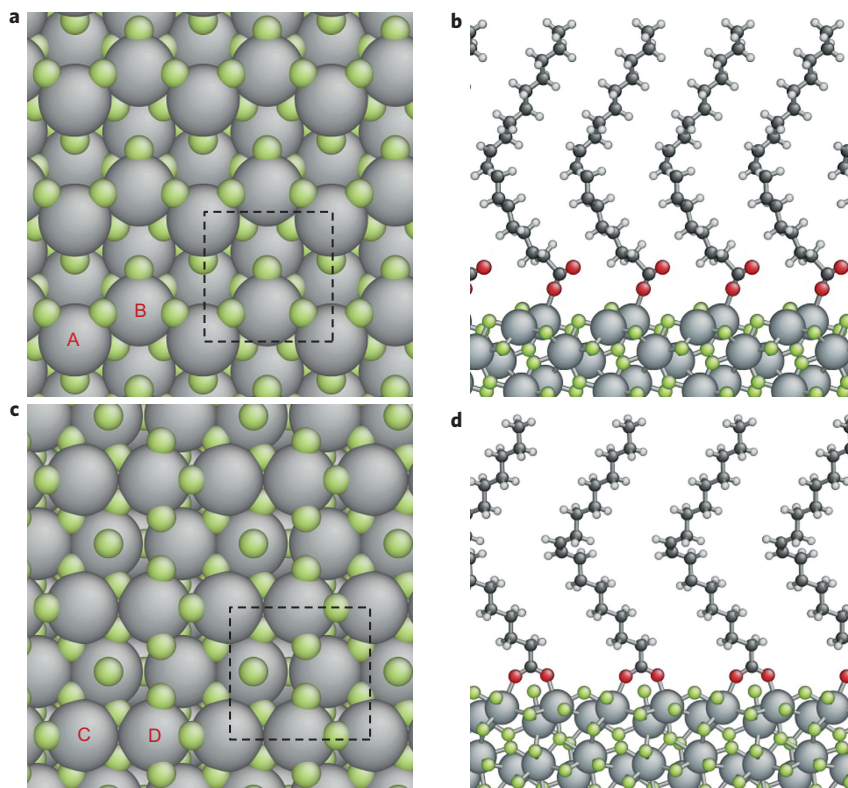


Figure 4 | Atomic structure of DyF_3 surfaces. **a-d**, DFT calculations revealed the structure of the (001) surface (**a,b**) and the (101) surface (**c,d**). The pristine surfaces are shown in the top view (**a,c**) and surfaces with adsorbed oleic acid are viewed from the side (**b,d**). The depicted atoms are Dy (grey), F (green), C (black), O (red) and H (white). The dashed squares in **a,c** are primitive unit cells on the surfaces. Letters A, B, C and D indicate different types of surface Dy atoms that have fewer nearest-neighbour F atoms than bulk Dy atoms. For each bulk Dy atom, there are nine nearest-neighbour F atoms. On the (001) surface, this number is seven for A and eight for B, and on the (101) surface both C and D have seven nearest-neighbour F atoms.

equilateral elongated hexagon. Hence, entropy alone always favours parallel alignment and never stabilizes an alternating pattern.

Density functional theory (DFT) calculations. To explain the appearance of the alternating arrangement for equilateral elongated hexagons, interparticle interactions were taken into account explicitly. We performed DFT calculations to assess the relative strength of van der Waals interactions between nanoplate edges induced by a difference in the coverage density of oleic acid ligands/tethers. As shown in Supplementary Section S3, the van der Waals interaction between the nanoplate inorganic cores can be neglected in the edge-to-edge configuration. Of particular interest is the atomistic origin of possible interaction anisotropies between the crystallographically distinct nanoplate edges, which we later identify as the reason for the formation of the alternating pattern.

We obtained the most-stable atomic structures of DyF_3 (001) and (101) surfaces (edges) by DFT calculations, as shown in Fig. 4a,c. We also calculated the surface dipoles of pristine edges and edges with adsorbed formate (HCOO). In both cases the dipoles on these two edges had similar values (Supplementary Section S2). This demonstrates that dipolar interactions cannot be responsible for edge-interaction anisotropy. Furthermore, zeta-potential measurements indicated that the LnF_3 nanoplates were nearly neutral, and therefore the contribution of electrostatic forces to the interparticle interactions was negligible (Supplementary Fig. S36). However, the surface atomic structures in Fig. 4a,c show that Dy atoms on the (101) edge have fewer nearest-neighbour F atoms than those on the (001) edge, which suggests that Dy atoms on the (101) edge should have a stronger adsorption ability than those on the (001) edge. Indeed, DFT calculations showed that

only one oxygen atom of each oleic acid molecule was coordinated to a Dy atom on the (001) edge, as opposed to two on the (101) edge (Fig. 4c,d and Supplementary Movies S5 and S6). As a result, the adsorption energy of oleic acid molecules on the (001) edge was 0.1 eV, compared to 0.7 eV on the (101) edge, which suggests a significant difference in the surface coverage density of oleic acid ligands between these two edges. Although DFT calculations were performed *in vacuo*, the calculated adsorption-energy difference should be robust regardless of the presence of solvents. In light of the large difference in adsorption energies, we believe that secondary solvent effects, such as an induced conformation change of alkyl chains of ligands³⁹, will not significantly change the relative effective interaction between different types of nanoplate edges.

Interaction asymmetry between nanoplate edges. We introduced an empirical model for the interaction between neighbouring particles for use in Monte Carlo simulations. As the particles do not possess significant charges or dipole moments, they interact only locally with an attractive van der Waals interaction induced by their oleic acid tethers (Fig. 5a). We further assumed that the interaction energy was linearly proportional to the contact area of the tethers, which means it was proportional to the edge-to-edge contact length in the 2D model. In our interaction model (see Methods and Supplementary Fig. S31) the potential energy was minimal for a parallel arrangement with neighbour distance equal to twice the tether length. It remained to choose an attraction strength ξ_{A-A} , ξ_{B-B} and ξ_{A-B} for each pair of edge types. For the equilateral elongated hexagon, by adding up all the neighbour contributions to the potential energy, we achieved a total energy difference $E_{\text{alt}} - E_{\text{para}} \propto 4\xi_{A-B} - 2\xi_{A-A} - 2\xi_{B-B}$. The alternating arrangement is preferred if the contact of unlike

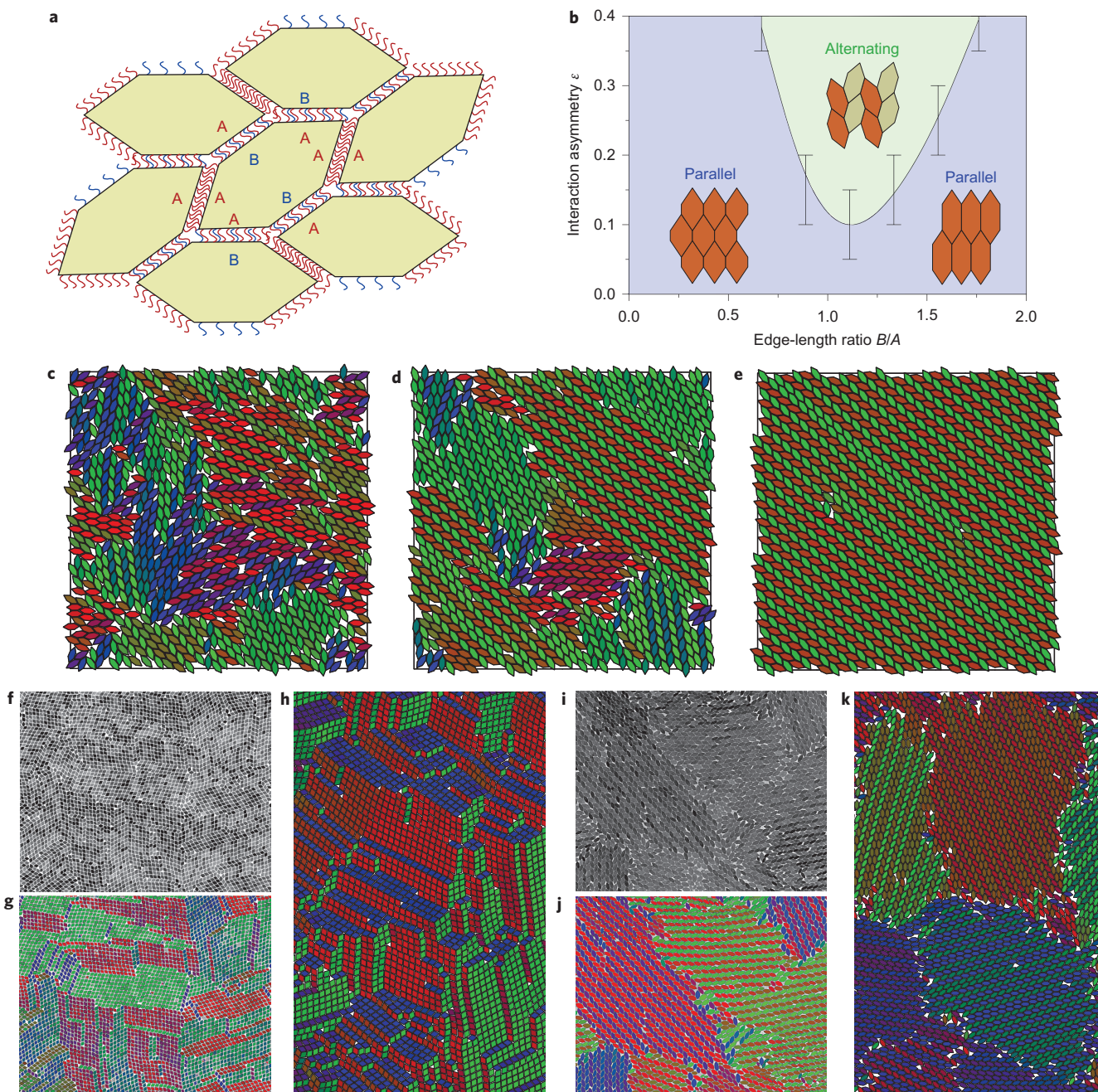


Figure 5 | Modelling and simulation of interacting lanthanide fluoride nanoplates. **a**, Oleic acid tethers cause an effective attraction of nanoplate edges that is asymmetric with respect to the two edge types A and B. **b**, The phase diagram as a function of edge-length ratio obtained from Monte Carlo simulations shows the stability regions of the parallel arrangement and the alternating arrangement. An interaction asymmetry greater than zero is required to stabilize the alternating arrangement. Error bars span from the lowest ε that exclusively forms the alternating arrangement to the highest ε that exclusively forms the parallel arrangement. **c–e**, Simulation results for the interaction asymmetry $\varepsilon = 0.2$ demonstrate the formation of the alternating arrangement (from left to right: early-, middle- and late-stage assembly). **f–k**, Electron microscopy snapshots in original contrast (**f–h**) and coloured using image processing (**g–j**) are compared to simulation results (**h–k**). A close similarity of the local order is apparent for $B/A = 0$ (**f–h**) and $B/A = 1$ (**i–k**).

edges is energetically advantageous, on average, compared to the contact of like edges, that is if the interaction asymmetry $\varepsilon (= 2\xi_{A-B}/(\xi_{A-A} + \xi_{B-B}) - 1) > 0$. Indeed, this was confirmed in the simulation (Fig. 5b). A slight preference for contact of unlike edges ($\varepsilon = 0.2$) resulted in alternating patterns (Fig. 5c–e, Supplementary Figs S32 and S33, and Supplementary Movie S4). The introduction of interactions to the rhomb system led to a polycrystal, which closely resembles the experimental results (Supplementary Fig. S34). For B/A either sufficiently greater or smaller than one, entropy dominated and the parallel

arrangement prevailed again. Fast compression of large systems resulted in polycrystalline assemblies with excellent agreement between simulations and experimental findings (Fig. 5f–k).

In close-packed nanocrystal superlattices, the interparticle distances can be regarded as an indication of the strength of van der Waals attractions that arise from partially interdigitated ligands that connect opposing edges. In the parallel arrangement of self-assembled superlattices of irregular hexagonal nanoplates, the B–B distance was consistently larger than the A–A distance regardless of the nanoplate aspect ratio (Supplementary Fig. S37). As

configurations in which the A–A distance was larger than the B–B distance and the reverse have very similar packing densities, they are entropically degenerate. Therefore, the experimentally observed non-uniformity in interparticle distances implies an asymmetry in the attractions between A–A and B–B edges. Finally, from DFT calculations we know that the B edges were much less covered by the oleic acid tethers compared to the A edges, which suggests $\xi_{\text{A}-\text{A}} > \xi_{\text{B}-\text{B}}$. However, A–B and A–A distances are very similar for nanoplates in the alternating arrangement (and are also close to the A–A distance in superlattices of rhombic nanoplates), which suggests $\xi_{\text{A}-\text{B}} \approx \xi_{\text{A}-\text{A}}$. The result is an interaction asymmetry $\varepsilon > 0$ (Supplementary Fig. S38).

Conclusions

In conclusion, we report here the synthesis of a family of highly faceted planar nanotiles with rich and subtle self-assembly behaviour. The aspect ratio of the nanoplates is tunable broadly by exploiting the trend of LnF_3 nanocrystal formation as a function of the type of lanthanide ions. Our results demonstrate that a combination of particle shape and directional attractions that result from the patchy coverage of ligands around the nanoplate edges is responsible for the self-assembly of nanocrystal superlattices different in structure from those that result from entropic forces alone. Controlled synthesis of shaped and faceted nanoplates not only enables the study of interplay between energy and entropy during self-assembly, but also provides further opportunity to amplify the interaction asymmetry through edge- and facet-selective chemical modification.

Methods

Nanocrystal synthesis. Lanthanide fluoride nanocrystals were synthesized using thermal decomposition of $\text{Ln}(\text{CF}_3\text{COO})_3$ in the presence of lithium salts ($\text{Li}(\text{CF}_3\text{COO})$ or LiF). Details are provided in Supplementary Sections S1 and S6.

Assembly of lanthanide fluoride nanocrystals into superlattices. A $1.5 \times 1.5 \times 1 \text{ cm}^3$ Teflon well was half-filled with ethylene glycol. Nanocrystal solution (15 μl) was drop-cast onto the ethylene glycol surface and the well was then covered by a glass slide to allow slow evaporation of hexane solvent. After 30 minutes, the nanocrystal film was transferred onto a TEM grid (300 mesh) and was further dried under vacuum to remove extra ethylene glycol.

Monte Carlo simulation. Nanoplates were represented as perfectly hard polyhedra. Checks for overlaps were performed as in Haji-Akbari *et al.*¹⁵ and Damasceno *et al.*¹⁶. A system of hard polyhedra was crystallized by slowly increasing the pressure until ordering was observed. Fast compression at the end of the simulation removed thermal disorder. Interacting nanoplates interacted via an attractive force (described below) in addition to hard-core repulsion. If interactions were present, then the pressure was kept fixed at the value at which the hard particle system crystallized and the temperature was decreased slowly until ordering occurred. We confirmed that the phase behaviour was not sensitive to the choice of pressure. System sizes ranged from 900 to 5,041 particles. Simulation times were typically several tens of millions of Monte Carlo cycles (in one cycle, each particle attempted to translate or rotate once on average). In simulation snapshots, particles were coloured according to their orientation. Free-energy calculations employed thermodynamic integration from an Einstein crystal (Frenkel–Ladd method for anisotropic hard particles).

Interaction model. Each pair of nanoplate edges with edge lengths l_1 and l_2 interacts via a pair potential chosen to mimic qualitatively the effect of oleic acid tethers. Indices were chosen such that $l_1 \geq l_2$. The potential energy depends on three parameters opening angle θ , parallel shift d_{\parallel} and normal distance d_{\perp} (see Supplementary Fig. S31). In this case, the potential energy separates as $V(\theta, d_{\parallel}, d_{\perp}) = -\xi V(\theta) V(d_{\parallel}) V(d_{\perp})$ with attraction strength $\xi > 0$ and

$$V(\theta) = 1 - \left(\frac{1 - \cos(\theta)}{1 - \cos(\theta_0)} \right)^2$$

$$V(d_{\parallel}) = \begin{cases} l_2, & \text{if } d_{\parallel} \leq (l_1 - l_2)/2 \\ (l_1 + l_2)/2 - d_{\parallel}, & \text{if } d_{\parallel} > (l_1 - l_2)/2 \end{cases}$$

$$V(d_{\perp}) = 1 - (1 - d_{\perp}/d_0)^2$$

for $\cos(\theta) < \cos(\theta_0) = 0.95$, $d_{\parallel} < (l_1 + l_2)/2$, $d_{\perp} < 2d_0 = 0.4 \text{ \AA}$ and 0 otherwise.

Image processing. TEM images that showed nanoplatelet assembly were processed using a 5×5 Sobel operator for edge detection. Regions of pixels with uniform contrast bounded by edges were identified as nanoplates. The particle orientation was determined from the direction of the largest eigenvalue of the inertia tensor. Particles were coloured according to a circular red–green–blue colour scheme.

DFT calculations. DFT calculations with spin-polarized conditions were performed using the Vienna *ab initio* simulation package (VASP) with a plane-wave basis set⁴⁰. Projector augmented wave (PAW) potentials with the Perdew–Burke–Ernzerhof (PBE) exchange–correlation functionals were used. The clean DyF_3 (001) and (101) surfaces were built from a fully relaxed bulk orthorhombic crystal structure with lattice constants $a = 6.341 \text{ \AA}$, $b = 6.764 \text{ \AA}$ and $c = 4.248 \text{ \AA}$. Detailed procedures for the calculations of optimized surface structures and the adsorptions of formate (HCOO) and oleate ($(\text{CH}_3(\text{CH}_2)_7\text{CH}=\text{CH}(\text{CH}_2)_7\text{COO})$) are described in Supplementary Section S2.

Received 26 October 2012; accepted 5 April 2013;
published online 12 May 2013

References

- Glotzer, S. C. & Solomon, M. J. Anisotropy of building blocks and their assembly into complex structures. *Nature Mater.* **6**, 557–562 (2007).
- Jones, M. R. *et al.* DNA-nanoparticle superlattices formed from anisotropic building blocks. *Nature Mater.* **9**, 913–917 (2010).
- Li, F., Josephson, D. P. & Stein, A. Colloidal assembly: the road from particles to colloidal molecules and crystals. *Angew. Chem. Int. Ed.* **50**, 360–388 (2011).
- Ye, X. *et al.* Morphologically controlled synthesis of colloidal upconversion nanophosphors and their shape-directed self-assembly. *Proc. Natl Acad. Sci. USA* **107**, 22430–22435 (2010).
- Langille, M. R., Zhang, J., Personick, M. L., Li, S. & Mirkin, C. A. Stepwise evolution of spherical seeds into 20-fold twinned icosahedra. *Science* **337**, 954–957 (2012).
- Zhang, Y. W., Sun, X., Si, R., You, L. P. & Yan, C. H. Single-crystalline and monodisperse LaF_3 triangular nanoplates from a single-source precursor. *J. Am. Chem. Soc.* **127**, 3260–3261 (2005).
- Saunders, A. E., Ghezelbash, A., Smilgies, D. M., Sigman, M. B. & Korgel, B. A. Columnar self-assembly of colloidal nanodisks. *Nano Lett.* **6**, 2959–2963 (2006).
- Shevchenko, E. V., Talapin, D. V., Kotov, N. A., O'Brien, S. & Murray, C. B. Structural diversity in binary nanoparticle superlattices. *Nature* **439**, 55–59 (2006).
- Leunissen, M. E. *et al.* Ionic colloidal crystals of oppositely charged particles. *Nature* **437**, 235–240 (2005).
- Yethiraj, A. & Van Blaaderen, A. A colloidal model system with an interaction tunable from hard sphere to soft and dipolar. *Nature* **421**, 513–517 (2003).
- Chen, Q., Bae, S. C. & Granick, S. Directed self-assembly of a colloidal kagome lattice. *Nature* **469**, 381–384 (2011).
- Macfarlane, R. J. *et al.* Nanoparticle superlattice engineering with DNA. *Science* **334**, 204–208 (2011).
- Bishop, K. J. M., Wilmer, C. E., Soh, S. & Grzybowski, B. A. Nanoscale forces and their uses in self-assembly. *Small* **5**, 1600–1630 (2009).
- Zhao, K., Bruinsma, R. & Mason, T. G. Entropic crystal-crystal transitions of Brownian squares. *Proc. Natl Acad. Sci. USA* **108**, 2684–2687 (2011).
- Haji-Akbari, A. *et al.* Disordered, quasicrystalline and crystalline phases of densely packed tetrahedra. *Nature* **462**, 773–777 (2009).
- Damasceno, P. F., Engel, M. & Glotzer, S. C. Crystalline assemblies and densest packings of a family of truncated tetrahedra and the role of directional entropic forces. *ACS Nano* **6**, 609–614 (2012).
- Agarwal, U. & Escobedo, F. A. Mesophase behaviour of polyhedral particles. *Nature Mater.* **10**, 230–235 (2011).
- Misztal, K. *et al.* Hierarchical self-assembly of suspended branched colloidal nanocrystals into superlattice structures. *Nature Mater.* **10**, 872–876 (2011).
- Henzie, J., Grünwald, M., Widmer-Cooper, A., Geissler, P. L. & Yang, P. Self-assembly of uniform polyhedral silver nanocrystals into densest packings and exotic superlattices. *Nature Mater.* **11**, 131–137 (2011).
- Bodnarchuk, M. I., Kovalenko, M. V., Heiss, W. & Talapin, D. V. Energetic and entropic contributions to self-assembly of binary nanocrystal superlattices: temperature as the structure-directing factor. *J. Am. Chem. Soc.* **132**, 11967–11977 (2010).
- Evers, W. H. *et al.* Entropy-driven formation of binary semiconductor–nanocrystal superlattices. *Nano Lett.* **10**, 4235–4241 (2010).
- Chen, Z., Moore, J., Radtke, G., Sirringhaus, H. & O'Brien, S. Binary nanoparticle superlattices in the semiconductor–semiconductor system: CdTe and CdSe. *J. Am. Chem. Soc.* **129**, 15702–15709 (2007).
- Chen, Z. & O'Brien, S. Structure direction of II–VI semiconductor quantum dot binary nanoparticle superlattices by tuning radius ratio. *ACS Nano* **2**, 1219–1229 (2008).
- Dong, A., Ye, X., Chen, J. & Murray, C. B. Two-dimensional binary and ternary nanocrystal superlattices: the case of monolayers and bilayers. *Nano Lett.* **11**, 1804–1809 (2011).

25. Damasceno, P. F., Engel, M. & Glotzer, S. C. Predictive self-assembly of polyhedra into complex structures. *Science* **337**, 453–457 (2012).
26. Jones, M. R., Macfarlane, R. J., Prigodich, A. E., Patel, P. C. & Mirkin, C. A. Nanoparticle shape anisotropy dictates the collective behavior of surface-bound ligands. *J. Am. Chem. Soc.* **133**, 18865–18869 (2011).
27. Glotzer, S. C. Nanotechnology: shape matters. *Nature* **481**, 450–452 (2012).
28. Bealing, C. R., Baumgardner, W. J., Choi, J. J., Hanrath, T. & Hennig, R. G. Predicting nanocrystal shape through consideration of surface-ligand interactions. *ACS Nano* **6**, 2118–2127 (2012).
29. Blunt, M. O. *et al.* Random tiling and topological defects in a two-dimensional molecular network. *Science* **322**, 1077–1081 (2008).
30. Stannard, A. *et al.* Broken symmetry and the variation of critical properties in the phase behaviour of supramolecular rhombus tilings. *Nature Chem.* **4**, 112–117 (2012).
31. Whitelam, S., Tamblyn, I., Beton, P. & Garrahan, J. Random and ordered phases of off-lattice rhombus tiles. *Phys. Rev. Lett.* **108**, 1–4 (2012).
32. Wang, F. *et al.* Simultaneous phase and size control of upconversion nanocrystals through lanthanide doping. *Nature* **463**, 1061–1065 (2010).
33. Zhao, K. & Mason, T. G. Twinning of rhombic colloidal crystals. *J. Am. Chem. Soc.* **134**, 18125–18131 (2012).
34. Zalkin, A. & Templeton, D. The crystal structures of YF_3 and related compounds. *J. Am. Chem. Soc.* **75**, 2453–2458 (1953).
35. Dong, A., Chen, J., Vora, P. M., Kikkawa, J. M. & Murray, C. B. Binary nanocrystal superlattice membranes self-assembled at the liquid–air interface. *Nature* **466**, 474–477 (2010).
36. Van der Kooij F. M., Kassapidou, K. & Lekkerkerker, H. M. W. Liquid crystal phase transitions in suspensions of polydisperse plate-like particles. *Nature* **406**, 868–871 (2000).
37. Paik, T., Ko, D.-K., Gordon, T. R., Doan-Nguyen, V. & Murray, C. B. Studies of liquid crystalline self-assembly of GdF_3 nanoplates by in-plane, out-of-plane SAXS. *ACS Nano* **5**, 8322–8230 (2011).
38. Stannard, A., Blunt, M. O., Beton, P. H. & Garrahan, J. P. Entropically stabilized growth of a two-dimensional random tiling. *Phys. Rev. E* **82**, 041109 (2010).
39. Roke, S., Berg, O., Buitenhuis, J., Van Blaaderen, A. & Bonn, M. Surface molecular view of colloidal gelation. *Proc. Natl Acad. Sci. USA* **103**, 13310–13314 (2006).
40. Kresse, G. & Furthmüller, J. Efficient iterative schemes for *ab initio* total-energy calculations using a plane-wave basis. *Phys. Rev. B* **54**, 11169–11186 (1996).

Acknowledgements

X.Y. and C.B.M. acknowledge support from the Office of Naval Research Multidisciplinary University Research Initiative on Optical Metamaterials through award N00014-10-1-0942. J.C. acknowledges support from the Materials Research Science and Engineering Center program of the National Science Foundation (NSF) under award DMR-1120901. C.B.M. is also grateful to the Richard Perry University Professorship for support of his supervisor role. M.E., J.A.M. and S.C.G. acknowledge support by the Assistant Secretary of Defense for Research and Engineering, US Department of Defense (N00244-09-1-0062). Any opinions, findings, and conclusions or recommendations expressed in this publication are those of the authors and do not necessarily reflect the views of the DOD/ASD (R&E), W.L., L.Q. and J.L. acknowledge support from the NSF (DMR-1120901). G.X. and C.R.K. acknowledge support from the US Department of Energy, Office of Basic Energy Sciences, Division of Materials Sciences and Engineering (Award DE-SC0002158). Correspondence and requests for materials should be addressed to S.C.G. and C.B.M.

Author contributions

X.Y. and J.E.C. carried out nanocrystal syntheses. X.Y. and J.C. performed nanocrystal self-assembly and structural characterization. M.E. conceived the Monte Carlo simulations. J.A.M. performed and analysed the Monte Carlo simulations. W.L. and L.Q. performed DFT calculations. G.X. conducted atomic force microscopy (AFM) characterization. S.C.G. and C.B.M. designed the study and supervised the project. All authors discussed the results and co-wrote the manuscript.

Additional information

Supplementary information is available in the online version of the paper. Reprints and permissions information is available online at www.nature.com/reprints. Correspondence and requests for materials should be addressed to S.C.G. and C.B.M.

Competing financial interests

The authors declare no competing financial interests.